Ionics (2011) 17:767–783
DOI 10.1007/s11581-011-0559-x

ORIGINAL PAPER

Study of thermal effects on the performance of micro-tubular solid-oxide fuel cells

Amin Mirahmadi · Kia Valefi

Received: 10 April 2010 / Revised: 8 March 2011 / Accepted: 5 April 2011 / Published online: 20 April 2011

Abstract Mathematical modeling of methane-fed anode-supported micro-tubular solid-oxide fuel cell (MT-SOFC) is developed. Steam reforming of methane is considered in two cases of: direct internal reforming (DIR) and gradual internal reforming (GIR). The polarization curves and temperature distribution of a cell fed with three variations of fueling (i.e., DIR and GIR of methane and pure hydrogen) are compared with each other. The simulation results are verified through temperature and performance measurements of a MT-SOFC sample operating on above three variations of fueling. In DIR operating condition, a drop in the anode gas temperature at a short distance after entering the cell takes place which results in high temperature gradient. In GIR operating condition, the temperature distribution in axial direction is steadier. The ohmic loss is lower in the case of pure hydrogen fuel than internal reforming of methane, but the concentration loss is lower in methane-fed operating conditions.

Keywords Micro-tubular SOFC · Reforming · Porous media · Heat transfer · Modeling

Nomenclature

A_v^E	Reactive surface area per unit volume of electrode ($m^2\ m^{-3}$)
c_i	Concentration of species: i (mol m^{-3})
c_{O_2}	Oxygen concentration (mol m^{-3})
c_{H_2}	Hydrogen concentration (mol m^{-3})
$c_{O_2,\mathrm{ref}}$	Oxygen reference concentration (mol m^{-3})
$c_{H_2,\mathrm{ref}}$	Hydrogen reference concentration (mol m^{-3})
c_p	Total heat capacity (J kg^{-1} K^{-1})
D_{eff}	Effective diffusion coefficient (m^2 s^{-1})
E_E	Apparent activation energy for the electrode reaction (J mol^{-1})
F	Faraday's constant (96,487 Cmol^{-1})
F_{amb}	Ambient view factor in radiative heat transfer
G_{m}	Mutual irradiation arriving from other surfaces in the modeled geometry (W m^{-2})
h_{i}	Enthalpy of species: i (J mol^{-1})
I	Cell average current density (A)
$\boldsymbol{I}$	Unit 3×3 matrix
J_i^E	Electrode normal ionic current flow (A m^{-2})
J_e^E	Electrode normal electronic current flow (A m^{-2})
J_0^E	Electrode reference exchange current density (A m^{-2})
$J_{0,\mathrm{ref}}^E$	Reference temperature current density (A m^{-2})
N_{D_i}	Species diffusion vector (mol m^{-2} s^{-1})
n_{CH_4}	Molar flow rate of the input fuel (mol s^{-1})
n_{air}	Molar flow rate of the input air (mol s^{-1})
n_{species}	Normal flux of species (mol m^{-2} s^{-1})
P	Pressure (Pa)
P_{species}	Partial pressure of species (Pa)
Q	Volumetric heat generation rate (J m^{-3})
q	Surface heat transfer (J m^{-3})
R	Universal gas constant (8.3143 Jmol^{-1} K^{-1})
t_{rl}^E	Reaction layer thickness (m)
T	Absolute temperature (K)
T_{amb}	Ambient temperature (K)
T_{ref}	Reference temperature for current density (K)
T_{g}	Gaseous phase temperature (K)
T_{s}	Solid-phase temperature (K)
U	Velocity vector (m s^{-1})
U_{gas}	Molar rate of gas consumption (mol s^{-1})
$\mathrm{UF}_{\mathrm{gas}}$	Gas utilization factor

A. Mirahmadi · K. Valefi (✉)
Department of Mechanical Engineering, Iran University of Science and Technology,
Narmak,
Tehran 16844, Iran
e-mail: kiavalefi@iust.ac.ir

Greek symbols

α_E	Symmetry factor (lies between 0 and 1)
ΔG^0	Standard Gibbs free energy change (J mol^{-1})
ΔH	Hydrogen high heating value (J mol^{-1})
ε	Surface emissivity in radiative heat transfer
ε_p	Porosity
ϕ_e	Electronic potential (V)
ϕ_i	Ionic potential (V)
κ	Porous layers permeability (m^2)
μ	Gas mixture viscosity (Pa s)
ρ	Gas mixture density (kg m^{-3})
σ	Stefan–Boltzman constant (5.67e–8 Wm^{-2} K^{-4})
σ_e	Electronic conductivity (S m^{-1})
σ_i	Ionic conductivity (S m^{-1})

Subscripts and Superscripts

E	Electrode
C	Cathode
A	Anode

Introduction

Solid-oxide fuel cells (SOFCs) are known as the most efficient devices for direct conversion of chemical energy of various gaseous fuels into electricity. They have several advantages over other types of fuel cells including flexibility of fuel used and relatively inexpensive material due to their high operating temperature [1]. There are two geometry types for SOFCs: planar-type SOFC and tubular-type SOFC. The tubular design mitigates the sealing problem at the elevated working temperature of SOFCs, but suffers from less effective electric current collection [2]. Micro-tubular solid-oxide fuel cells (MT-SOFC) with millimeter to sub millimeter diameter, provide an excellent approach to developing rapid start-up of SOFCs, due to their high strength, resistance to thermal shocks, and high power densities especially in small diameters [3]. Considering MT-SOFC advantages, it is even suggested that the presumption that the SOFC technology could not meet the requirements needed by a vehicle power plant (i.e., reduced size, high power density, and rapid start-up) may be incorrect [4].

Cost, reliability, and durability are important parameters in design and commercializing all types of SOFCs [5]. Also, rapid start-up and power density are important problems in widespread application of SOFCs. In these respects, sealing, manifold design, optimization of the fuel, and oxidant flow regimes and electrical connections comprise basic challenges in making the MT-SOFCs commercialized [3]. A thorough understanding of thermal effects of such phenomena as hydrocarbon reforming, electrochemical reactions, conductive, convective, and radiative heat transfer are crucial in improving SOFC durability. SOFCs can stably operate by such fuels as methanol or methanoic acid which can be easily steam reformed by the nickel anode at the working elevated temperature [6]. Recently, there have been increasing studies on direct operation of SOFC (without a prereformer) on short-chain hydrocarbons (HC) such as methane (which is readily available in natural gas) and butane. This reduces operating cost and entails higher efficiency. The major challenge of direct reforming of HCs in SOFCs is that deposit of carbon on the nickel anode particles surface deteriorates the anode performance as a catalyst for electrochemical reactions [7].

Supplying enough heat to the methane reforming reaction and preserving a minimum value of 2 for the steam to carbon ratio (i.e., molar ratio of steam to atomic carbon) at the reformer inlet guarantee that the atomic carbon is not formed in the reactor [8]. There are two approaches for internal reforming SOFC (IR-SOFC), i.e., direct internal reforming SOFC (DIR-SOFC) and indirect internal reforming SOFC (IIR-SOFC). In the first method, exothermic electrochemical reaction provides the necessary heat for endothermic reforming reaction which occurs simultaneously at the SOFC anode. Therefore, the anode material for DIR-SOFC should be optimized for both reactions since it is subjected to poisoning by carbon deposition from hydrocarbon reforming [9]. In IIR-SOFC, reforming occurs at a separate place in thermal contact to SOFC anode, so the problem of carbon deposition is mitigated. However, problems such as local temperature reduction which is also magnified due to the mismatch of the two reaction rates induces high thermal stresses especially at the reformer inlet [10]. Application of catalyst with low reforming activity has been proposed as a remedy for the mismatch of the reaction rates [11]. The combination of steam reforming and partial oxidation which is called autothermal reforming results in more even temperature distribution at the reformer since it reduces the required external heat [12].

Gradual internal reforming (GIR) is another approach for reduction of temperature gradient in the SOFC anode. In this method, the mole fraction of steam supplied to methane input to reformer is not sufficient to accelerate the steam reforming reaction. Therefore, the steam and heat provided from electrochemical reaction increase the electrochemical reaction rate gradually [13,14].

Numerical modeling provides an effective facility to predict states of the fuel cell operation conditions such as temperature distributions and partial pressure of gasses. Temperature distribution, the cell performance, and internal reforming reaction kinetics are such correlated to each other that a thorough study on the performance of a MT-SOFC must comprise all of them. Some researchers developed models for DIR in the SOFC anode, e.g., one-dimensional model with geometry integration and mass transport [15], models developed to study the effect of various diffusion formulations on the concentration loss [16], mass transfer, and electric potential distribution within electrodes and electrolyte [17]. In these models, it has been assumed that the reforming reaction occurs at the porous anode and the electrochemical reaction takes place at the interface boundary of anode and electrolyte. In models developed to simulate GIR-SOFC, the necessary hydrogen for electrochemical reaction is generated in situ. So, steam concentration is a predominant parameter in the reaction kinetics. Modeling of an electrolyte-supported tubular SOFC fueled by methane with DIR and GIR operations and using finite volume method was studied by Klein et al. [18] to account the experimental results presented by Georges et al. [14].

The present study proposes a numerical model for an anode-supported MT-SOFC operating on methane and pure hydrogen. Two variations are considered for the internal reforming, i.e., DIR and GIR. The cell performance is predicted through simultaneous solution of the momentum, species diffusion, heat transfer, reforming, and electrochemical equations. The exactness of the developed model in prediction of temperature field is checked by simple temperature measurements of manufactured MT-SOFC sample.

Experimental

Cell manufacturing

The MT-SOFC sample which was considered to study the temperature distribution had the geometry and dimensions as shown in Fig. 1. The sample diameter was chosen in the upper limit of MT-SOFCs (i.e., 14.6 mm) in order to facilitate the installation of four thermocouples at axial coordinates: 10, 30, 70, and 120 mm as shown in Fig. 2. The manufacturing process of tested MT-SOFC is summarized in Fig. 3. The nickel-8YSZ cermet supporting tube was manufactured by slurry method in which a mixture of 40 wt.% nickel oxide (d≤1 μm), 40 wt.% 8YSZ (d≤1 μm) and 20 wt.% 8YSZ (25 μm≤d≤40 μm) powders were ball milled for 8 h with an aqueous solution of ethyl vinyl alcohol and stearic acid. The ball-milled suspension was poured in a plaster mold to the designed tubular shape. After drying, the electrolyte layer was produced through dip coating the green support in a slurry of 8YSZ (8YSZ powder, d≤1 μm mixed in an aqueous solution of ethyl vinyl alcohol and stearic acid). After co-sintering the supporting tube and electrolyte layers in 1,450°C for 6 h, the cathode layer was produced by solution precursor plasma spraying technique in which a solution consisting of lanthanum, strontium, and manganese nitrates to a proportion resulting $La_{0.8}Sr_{0.2}MnO_3$ was sprayed by an air atomizer to the high temperature zone of a Plasma Techniques–Gun F4 which resulted in vaporization of water content of the nitrates solution, pyrolysis, and formation of a porous thermally sprayed cathode layer.

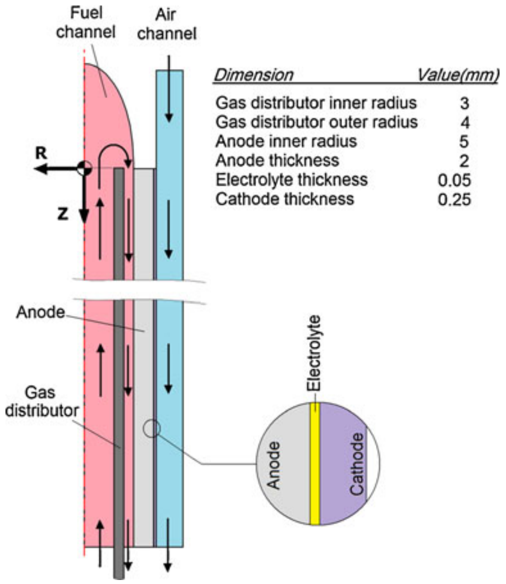

Fig. 1 Micro-tubular solid-oxide fuel cell geometry and dimensions

Cell testing

The prepared cell was tested in an apparatus which is depicted in Fig. 2. The input gasses were preheated in heat exchangers, each were consisted of 60 turns of 4 mm outside diameter stainless steel pipe, wrapped around 80 mm inner diameter coils. Therefore, the temperature of fuel and air input to the cell were nearly the same as the furnace temperature. The temperatures at four points along the cell were acquired by insertion of chromel–alumel thermocouples in contact with the cell cathode. The electric current was collected from the cathode layer by stainless steel (with chemical composition presented in Table 1) string (mesh 200) and from inner diameter of the anode by the same grade of stainless steel spring (1-mm wire diameter and 5-mm pitch). The wires which were connected to these collectors also were of the same grade of stainless steel in order to reduce contact resistance due to oxidation.

Air and methane flow to the cell were metered by ordinary gas flow meters of the rotameter type. Water was sprayed to the anode input gas stream in an electrically preheated chamber to prevent its separation from the stream which might take place by wetting the tube wall.

All of the experimental data were analyzed to investigate the effects of metrological uncertainty. The errors of temperature and voltage measurement systems were directly

Fig. 2 MT-SOFC testing setup

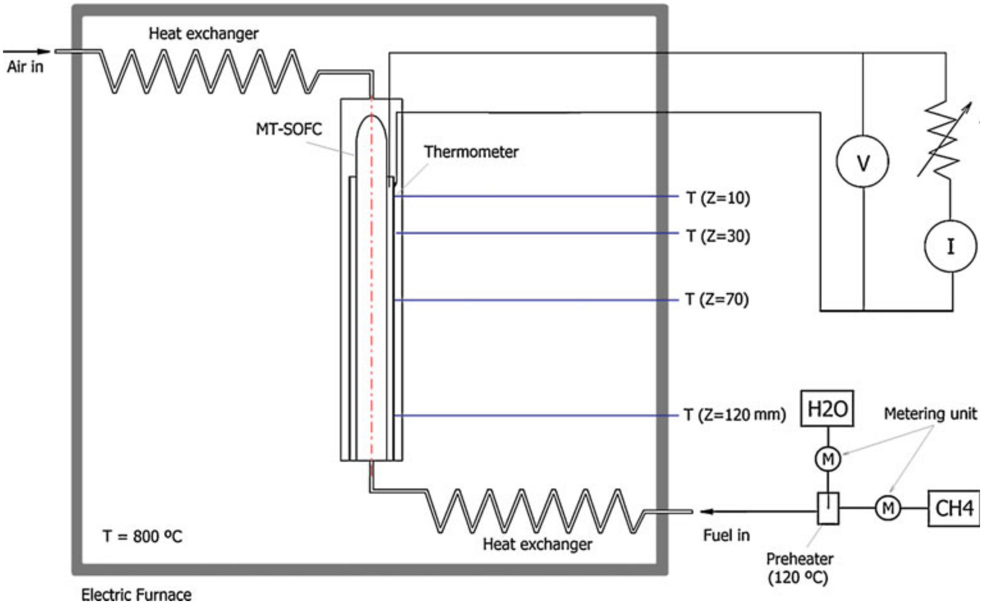

applicable to the uncertainty analysis. However, to analyze the effects of gas flow rates and electrical current measurement errors, some sensitivity analyses were performed on polarization and temperature curves. The results of uncertainty analyses are depicted in graphs of experimental data considering a coverage factor of 2.

Model description

Geometry

The whole radial section shown in Fig. 1 is considered as the computational domain for the axial symmetric problem. The computational domain is bounded by the inner wall of a surrounding tube in radial direction.

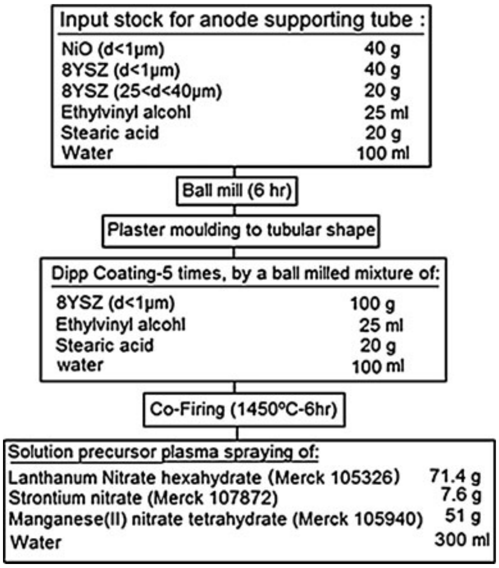

Fig. 3 Manufacturing process of tested MT-SOFC sample

Assumptions

In the electrical model, for the positive cathode, electrolyte and negative anode (PEN) layers isotropic electrical or ionic conductivity was considered. As depicted in Fig. 4, due to large electrical conductivity of the interconnects, ideal current collection was assumed at the cathode outer and anode inner boundaries which would imply constant electrical potentials at those surfaces [19]. The independence of electric current densities at outer and inner diameters of the cell from the cylindrical angular coordinate provides the model with the facility of axial symmetry assumption.

All of the physical models presented in this paper are aimed at prediction of the steady state operation of the MT-SOFC and time dependent phenomena are neglected. The gas species diffusion was expressed by Fick's law [19]. Also, ideal gas behavior was assumed for the fuel and air at the operating temperature of MT-SOFC. Other assumptions are expressed where the related physical models are explained in the following sections. The momentum equations for the laminar flow of ideal gasses are governing in the air and fuel channels as Navier–Stokes equations [20] and in the porous layers of anode and cathode as Brinkman's equations [21]. The species diffusion equations regulate the air and fuel channels and also porous cathode and anode layers [22]. The Ohm's law is

Table 1 Chemical composition of stainless steel current collectors

Fe	C	Mn	P	S	Si	Cr
Bal.	0.14	0.71	0.03	0.01	0.28	12.43

Fig. 4 The governing equations and boundary conditions for the electrical model

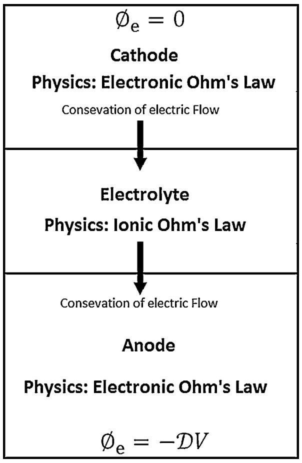

solved in the cathode and anode layers to account for the conservation of electronic charge and in the electrolyte layer to account for the conservation of ionic charge. The gaseous phase heat transfer is comprised of diffusive and convective heat fluxes along with heat conduction in the domain and heat convection at the boundaries with solid phases [19]. In the porous solid-phase, heat transfer is consisted of conduction in the domain and convection and radiation at the boundaries with gas channels [23]. Aside from the boundaries, at the porous subdomains, gaseous and solid-phases exchange heat with each other which is considered through volumetric heat input terms with opposite signs [24].

Electrical model

The governing physics and boundary conditions for the electrical model are summarized in Fig. 4. In the cathode and anode electrodes, the conservation of electronic charges is expressed in the form of Ohm's law as:

$$\nabla \cdot (\sigma_e \nabla \phi_e) = 0 \tag{1}$$

Where σ_e is electronic conductivity of the cathode or anode electrode and ϕ_e is the electronic potential. In the electrolyte layer, the conservation of oxygen ion (O^{2-}) charges is written in the form of Ohm's law as:

$$\nabla \cdot (\sigma_i \nabla \phi_i) = 0 \tag{2}$$

Where σ_i is ionic conductivity of the electrolyte layer, and ϕ_i is the ionic potential. For the ionic Ohm's law, as depicted in Fig. 4, at the interface of electrolyte with the electrodes the boundary conditions consist of the equivalence of ionic current flow to electronic current flow in the direction normal to the boundary:

$$J_i^C = J_e^C \tag{3}$$

$$J_i^A = J_e^A \tag{4}$$

Where J_i^A, J_i^C, J_e^A, and J_e^C are ionic and electronic currents in normal directions to the boundaries. For the electronic Ohm's law, at the interface of electrolyte with the electrodes the boundary conditions are:

$$\phi_e = \phi_i + V_{\mathrm{rev}}^C - \eta_C \tag{5}$$

$$\phi_e = \phi_i + V_{\mathrm{rev}}^A + \eta_A \tag{6}$$

Where:

$$V_{\mathrm{rev}}^A = \frac{\Delta G^0}{2F} - \frac{RT}{2F}\ln\left(\frac{p_{\mathrm{H_2}}}{p_{\mathrm{H_2O}}}\right) \tag{7}$$

$$V_{\mathrm{rev}}^C = \frac{RT}{4F}\ln\left(\frac{p_{\mathrm{O_2}}}{p_0}\right) \tag{8}$$

In which, ΔG^0 and F denote the standard Gibbs free energy change and Faraday's constant, $P_{\mathrm{H_2}}$, $P_{\mathrm{H_2O}}$, $P_{\mathrm{O_2}}$, and P_0 denote, hydrogen, water steam, oxygen partial pressures, and atmospheric pressure, respectively. η_C and η_A denote activation losses at the cathode and anode reaction zones (Eqs. 11 and 12).

Electrochemical model

The electrochemical reactions taking place in the cathode and anode reaction zones are:

$$\mathrm{O_2} + 4\mathrm{e}^- \rightarrow 2\mathrm{O}^{2-} \tag{9}$$

$$2\mathrm{H_2} + 2\mathrm{O}^{2-} \rightarrow 2\mathrm{H_2O} + 4\mathrm{e}^- \tag{10}$$

The current densities in the cathode and anode reaction zones (which are considered the interface of electrolyte with electrodes) are expressed in the form of Butler–Volmer equations in a manner similar to that used by Hussain et al. [25]:

$$J_e^C = J_0^C A_v^C t_{rl}^C \left(\frac{c_{\mathrm{O_2}}}{c_{\mathrm{O_2,ref}}}\right)^{\gamma_{\mathrm{O_2}}} \left[\exp\left(\frac{\alpha_c n_c F \eta_c}{RT}\right) - \exp\left(-\frac{(1-\alpha_c) n_C F \eta_C}{RT}\right)\right] \tag{11}$$

$$J_e^A = \mathrm{J}_0^A A_v^A t_{rl}^A \left(\frac{c_{\mathrm{H_2}}}{c_{\mathrm{H_2,ref}}}\right)^{\gamma_{\mathrm{H_2}}} \left[\exp\left(\frac{\alpha_A n_A F \eta_A}{RT}\right) - \exp\left(-\frac{(1-\alpha_A) n_A F \eta_A}{RT}\right)\right] \tag{12}$$

The superscript: E (electrode) denotes C (cathode) or A (anode), then J_e^E is the electrode current density, J_0^E is the electrode reference exchange current density which can be acquired at reference oxygen concentration: $c_{\mathrm{O_2,ref}}$ and reference hydrogen concentration: $c_{H_2,\mathrm{ref}}$. c_{O_2} and c_{H_2} are oxygen and hydrogen molar concentrations, γ_{O_2} and γ_{H_2} are reaction orders for oxygen reduction and hydrogen oxidation, respectively. A_v^E is reactive surface area per unit volume which is expressed by Costamagna et al. [26]. t_{rl}^E is the reaction layer thickness, α_E is the symmetry factor whose value lies between 0 and 1, n_E denotes the number of electrons participating in the electrochemical reaction (2 for hydrogen oxidation and 4 for oxygen reduction), R is the universal gas constant, and T is the absolute temperature.

With a value of 0.5 for the symmetry factors and reaction orders, Eqs. 11 and 12 are simplified for the activation losses as below:

$$\eta_C = \frac{RT}{0.5n_C F}\sinh^{-1}\left[\frac{J_e^C}{2J_0^C A_v^C t_{rl}^C \left(\frac{C_{O_2}}{C_{O_2,\mathrm{ref}}}\right)^{0.5}}\right] \tag{13}$$

$$\eta_A = \frac{RT}{0.5n_A F}\sinh^{-1}\left[\frac{J_e^A}{2J_0^A A_v^A t_{rl}^A \left(\frac{C_{H_2}}{C_{H_2,ref}}\right)^{0.5}}\right] \tag{14}$$

Which are substituted in Eqs. 5 and 6. For expressing the temperature dependence of J_0^E, predefined Arrhenius expression is used:

$$J_0^E = J_{0,\mathrm{ref}}^E \exp\left[\frac{-E_E}{R}\left(\frac{1}{T} - \frac{1}{T_{\mathrm{ref}}}\right)\right] \tag{15}$$

Where $J_{0,\mathrm{ref}}^E$ denotes current density at reference temperature, E_E is the apparent activation energy for the electrode reaction, and T_{ref} is the reference temperature.

Momentum conservation model

In the fuel and air channels momentum conservation is expressed in the form of Navier–Stokes equations as:

$$\rho\mathbf{u}.\nabla\mathbf{u} = \nabla.[-p\mathbf{I} + \mu(\nabla\mathbf{u} + (\nabla\mathbf{u})^T)] \tag{16}$$

In the porous cathode and anode layers, the momentum equation is written in the form of Brinkman equations [27] as:

$$(\mu/\kappa)\mathbf{u} = \nabla.[-p\mathbf{I} + (1/\varepsilon_p)\mu(\nabla\mathbf{u} + (\nabla\mathbf{u})^T)] \tag{17}$$

Where ρ is the gas mixture density, $\mathbf{u}$ the velocity vector, p the pressure, $\mathbf{I}$ the unit 3×3 matrix, μ the gas mixture viscosity, κ permeability of porous layers, and ε_{p} denotes porosity of these layers. The boundary conditions for the momentum conservation equations are comprised of volumetric flow rates at channels outputs and specified pressures at channels inputs.

Mass transport

Mass transport in gas channels and porous layers takes place with convective as well as diffusive fluxes which the later is explained by the Fick's law. Therefore, conservation of mass is expressed as:

$$\nabla.(-D_{\mathrm{eff}}\nabla c_i) + \mathbf{u}.\nabla c_i = 0 \tag{18}$$

Where D_{eff} which denotes the effective diffusion coefficient is explained by Chan et al. [28], c_i is the i*th* species concentration. Therefore, equation set (18) consists of as many equations as number of species.

The boundary conditions for the mass transport model consist of constant species concentrations at the input to channels and convective flux at the outputs. At interface of electrodes with the electrolyte following normal fluxes exist:

$$n_{H_2} = -\frac{J_A^e}{2F} \tag{19}$$

$$n_{H_2O} = \frac{J_A^e}{2F} \tag{20}$$

$$n_{O_2} = -\frac{J_C^e}{4F} \tag{21}$$

Where n_{H_2}, n_{H_2O}, and n_{O_2} denote normal molar fluxes of: H_2, $\mathrm{H_2O}$, and $\mathrm{O_2}$, respectively.

Heat transfer

Heat transfer equation is expressed in the general form:

$$\nabla.(-k\nabla T + \sum\nolimits_i h_i N_{D_i}) = Q - \rho c_p\mathbf{u}.\nabla T \tag{22}$$

Where h_i denotes enthalpy of the species: i, N_{D_i} is the diffusive flux vector of species: i, c_p is the heat capacity, and Q is the volumetric heat input. For gaseous phases, porous electrodes, dense electrolyte, and dense solid gas distributor, the terms in Eq. 22 are denoted in Table 2. In this table, the terms $J_e.\nabla\phi_e$ and $J_i.\nabla\phi_i$ represent volumetric electrical heating terms, where J_e and J_i are electronic and ionic current density vectors. $h_v(T_{\mathrm{s}} - T_{\mathrm{g}})$ is convective heat transfer from unit volume of porous electrode solid phase to diffusive gaseous phase [29]. The term $(-R_1\Delta h_1 + R_2\Delta h_2)$ denotes the cooling effect due to

Table 2 Terms of Eq. 20 in various phases

	T	N_{D_i}	u	Q
Fuel gas	T_g	$-D_{\mathrm{eff}}\nabla c_i$	u	$h_v(T_s - T_g) - R_1\Delta h_1 + R_2\Delta h_2$
Air	T_g	$-D_{\mathrm{eff}}\nabla c_i$	u	$h_v\left(T_s - T_g\right)$
Porous electrode	T_s	0	0	$h_v(T_s - T_g) + J_e\nabla\phi_e$
Solid gas distributor	T_s	0	0	0
Solid electrolyte	T_s	0	0	$J_i\nabla\phi_i$

methane reforming per unit volume of the porous anode, as expressed in (Eqs. 27–31).

The boundary conditions of the heat transfer problem consist of convective heat transfer between solid electrolyte and diffusive gaseous phase in porous electrodes, between the solid phase of porous electrodes and gasses flowing in the channels and between solid gas distributor and fuel gas flowing in the fuel channel. Also, radiative heat transfer was considered between the inner wall of anode and gas distributor and between the cathode outer wall and ambient as:

$$q = \varepsilon\left(G - \sigma T^4\right) \tag{23}$$

Where ε is emissivity of the surface, σ is the Stefan–Boltzman constant, and G is total arriving radiative flux or irradiation which is expressed as:

$$G = \sigma T_{\mathrm{amb}}{}^4 \tag{24}$$

For surface to ambient heat radiation, and:

$$G = G_m + F_{\mathrm{amb}}\sigma T_{\mathrm{amb}}^4 \tag{25}$$

For surface to surface heat radiation [18], G_m is mutual irradiation arriving from other surfaces in the modeled geometry, F_{amb} is ambient view factor, and T_{amb} is the ambient temperature where in this study was considered as the furnace temperature.

At the interface of electrolyte and anode, the heat generation term in W m^{-2} to account for irreversibility of electrochemical reactions is expressed as:

$$q = \left(\frac{\Delta H}{2F} - \left(V_{\mathrm{rev}}^{C} - V_{\mathrm{rev}}^{A}\right)\right)J_e^A \tag{26}$$

Where ΔH is hydrogen high heating value.

Fuel reforming

At the operating temperature of SOFC, methane reforming is possible at porous nickel-YSZ cermet anode as a catalyst. The complete reforming reaction is:

$$CH_4 + 2H_2O \rightarrow 4H_2 + CO_2 \tag{27}$$

This reaction is comprised of two reactions:

$$CH_4 + H_2O \leftrightarrow 3H_2 + CO \quad \left(\Delta h_1 = 206\ \mathrm{kJ\ mol^{-1}}\right) \tag{28}$$

$$CO + H_2O \leftrightarrow H_2 + CO_2 \quad \left(\Delta h_2 = -41\ \mathrm{kJ\ mol^{-1}}\right) \tag{29}$$

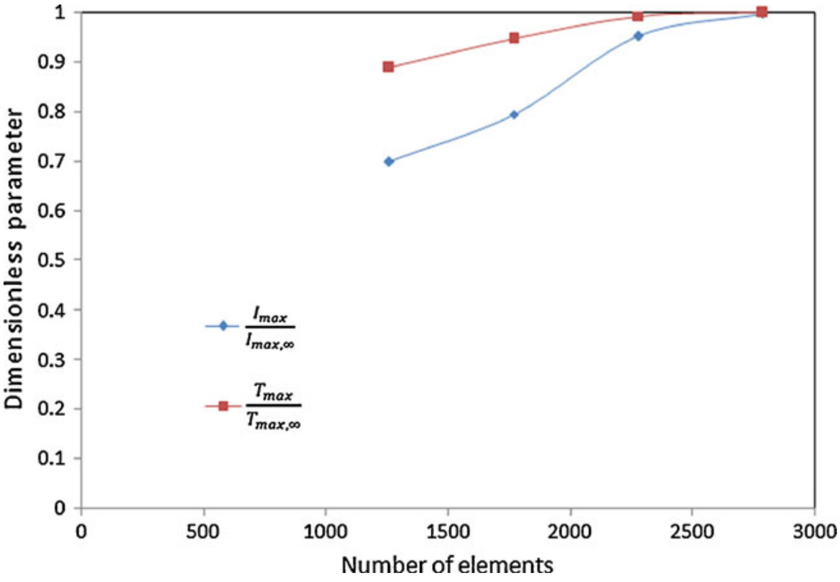

Fig. 5 Mesh sensitivity analysis results

Table 3 Parameters used in the simulation

Parameters	Values	Reference
Operation conditions		
Fuel/air utilization factor	0.40/0.17	[35]
Input fuel/air temperature (°C)	800/800	
Input c_{H_2O}/c_{CH_4} in GIR operation	0.094	[30]
Input c_{H_2O}/c_{CH_4} in DIR operation	1.23	[30]
Output fuel/oxygen pressure (bar)	1.013	
Cathode/anode		
Reference current density (Am^{-2})	400/1,320	[25]
Apparent activation energy (kJ mol^{-1})	130/120	[31]
Reference temperature (K)	1073/1073	[31]
Reference concentration (mol m^{-3})	2.38/10.78	[25]
Electrical conductivity (S m^{-1})	5,376/71,428	[25]
Thermal conductivity (W m^{-1} K^{-1})	6.0/11.0	[32]
Porosity	0.35	[25]
Density (kg m^{-3})	4,930.0/4,460.0	[32]
$A_v^E (m^2 m^{-3})$	80,625	[26]
$t_E^{rl} (m)$	20e–6	[26]
Other parameters		
Electrolyte ionic conductivity (S m^{-1})	$(1.93e8/T)\exp(-103,000/RT)$	[33]
Electrolyte thermal conductivity (W m^{-1} K^{-1})	2.7	[32]
D_{eff} (m^2 s^{-1})	$0.308\exp(-11,000/T)$	[34]
Thermal conductivity of support (W m^{-1} K^{-1})	11.0	[32]
Thermal conductivity of air tube (W m^{-1} K^{-1})	11.0	[32]
Thermal emissivity of preheating tube	0.05	[23]
Thermal emissivity of electrodes	0.35	[23]

Reaction of Eq. 28 known as methane steam reforming (MSR), is highly endothermic and reaction of Eq. 29 known as water gas shift reaction (WGSR), is a little exothermic. Molar rate of the MSR reaction in (mol m^{-2} s^{-1}) is described by the Arrhenius law [18] as:

$$R_{MSR} = 63.6 \times T^2 \times \exp\left(-\frac{27,063}{T}\right)[CH_4][H_2O] - 3.7 \times 10^{-14} \times T^4 \times \exp\left(-\frac{232.78}{T}\right)[CO][H_2]^3 \quad (30)$$

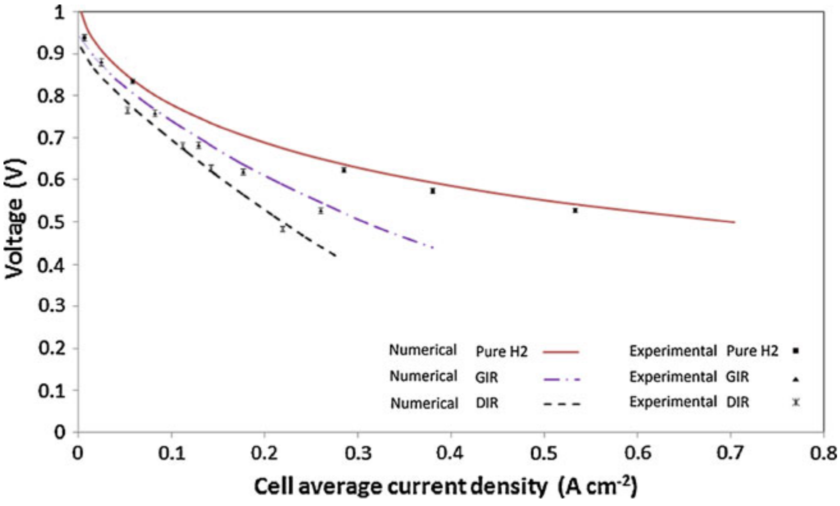

Fig. 6 Polarization curves of the MT-SOFC for various fueling methods

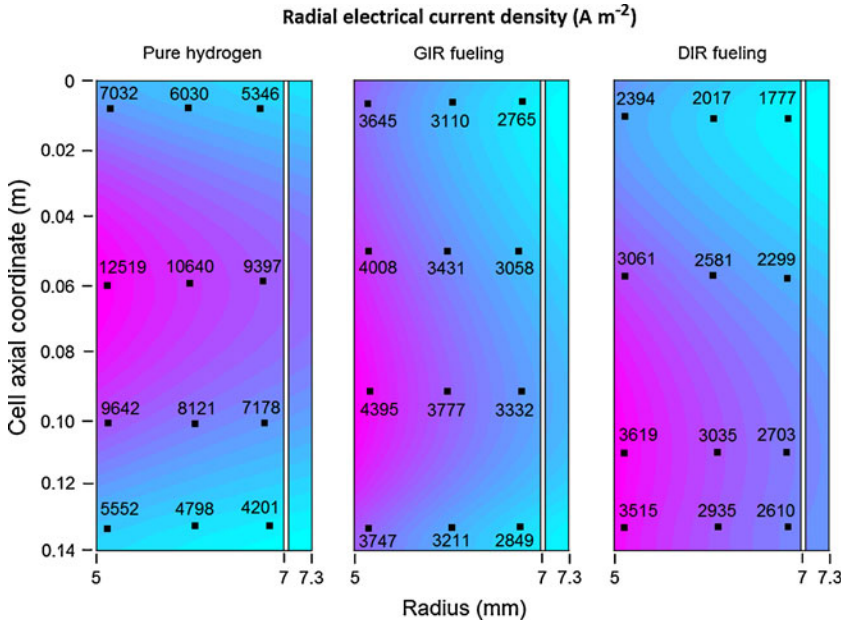

Fig. 7 Numerical results of radial electrical current density contours at the cell operating voltage of 0.5 V

Where [*g*] denotes the concentration of gas species: *g*. Unlike the MSR reaction, WGSR occurs wherever the gas is present with a molar rate in (Kmol m^{-3} s^{-1}) as:

$$R_{\mathrm{WGSR}} = 1,192 \times T^2 \times \exp\left(-\frac{12,509}{T}\right)[\mathrm{CO}][\mathrm{H_2O}] - 6.77 \times 10^4 \times T^2 \times \exp\left(-\frac{16,909}{T}\right)[\mathrm{CO_2}][\mathrm{H_2}] \tag{31}$$

The molar fluxes of species in (mol m^{-2} s^{-1}) satisfy the differential equations:

$$\nabla N_{\mathrm{CH_4}} = -A_v^A R_{\mathrm{MSR}} \tag{32}$$

$$\nabla N_{\mathrm{H_2O}} = -A_v^A R_{\mathrm{MSR}} - R_{\mathrm{WGSR}} \tag{33}$$

$$\nabla N_{\mathrm{CO}} = A_v^A R_{\mathrm{MSR}} - R_{\mathrm{WGSR}} \tag{34}$$

$$\nabla N_{\mathrm{H_2}} = 3A_v^A R_{\mathrm{MSR}} + R_{\mathrm{WGSR}} \tag{35}$$

$$\nabla N_{\mathrm{CO_2}} = R_{\mathrm{WGSR}} \tag{36}$$

Where N_i denotes molar flux vector of species: i.

In addition to reactions (28) and (29), pyrolysis (Eq. 37) and Boudouard (Eq. 38) reactions may also take place.

$$\mathrm{CH_4} \rightarrow C + 2\mathrm{H_2} \qquad (\Delta \mathrm{h} = 75\ \mathrm{kJ\ mol^{-1}}) \tag{37}$$

$$2\mathrm{CO} \rightarrow \mathrm{C} + \mathrm{CO_2} \qquad (\Delta \mathrm{h} = -172.6\ \mathrm{kJ\ mol^{-1}}) \tag{38}$$

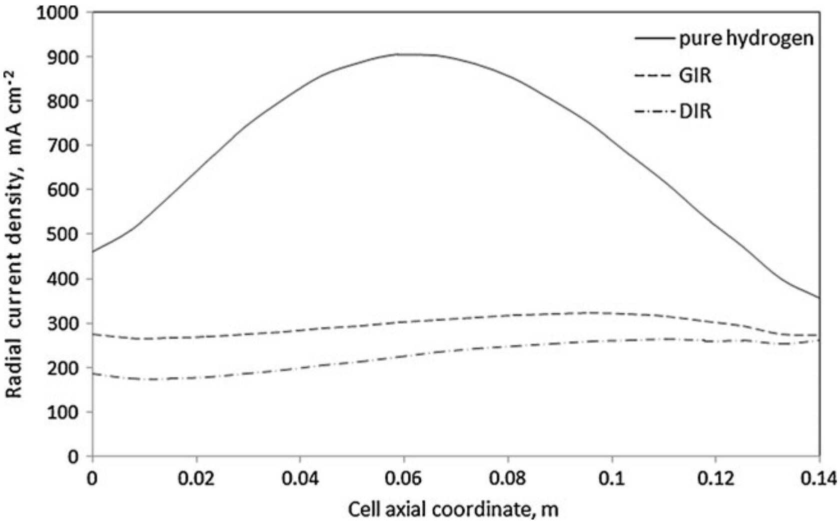

Fig. 8 Numerical results of radial current density at the anode-electrolyte interface at the cell operating voltage of 0.5 V

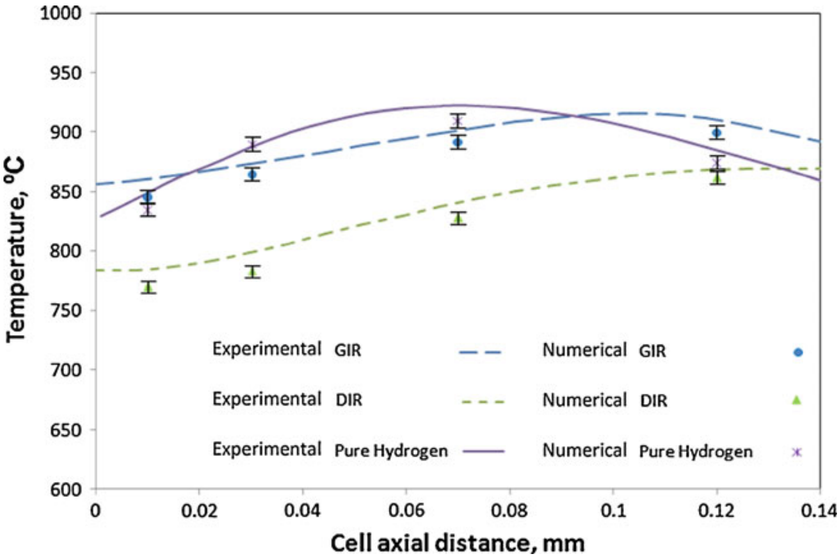

Fig. 9 Numerical results of temperature profile at the electrolyte mid-thickness of the MT-SOFC for various fueling methods

Previous work on methane reforming implied that for a steam to carbon, STC, ratio larger than 2.0 the probability of formation of atomic carbon is very low. However, a high value of STC ratio dilutes the hydrogen being formed. An analysis of the Gibbs free energy change of (Eqs. 28–38) denotes that for temperatures above 1,000 K (750°C) methane has more likely to react with steam to form hydrogen according to Eq. 28 than dissociate into atomic carbon and water. This tendency is enhanced by high concentration of water [8]. Therefore, as in the present study the operating temperature of the MT-SOFC is higher than 1,000 K (Eqs. 37 and 38) are disregarded in the model.

Simulation implementation

Computational technique

The necessary formulations for the models presented in this paper were supplied to the finite element software package FEMLAB® [27]. The geometric modeling and meshing were based on the axial symmetry assumption. The current collection was assumed to be ideal, so constant electric potentials of 0 and –DV were specified on cathode outer surface and anode inner surface at each steady state simulation run. Electric and ionic current densities, electric potential distribution, species concentrations, velocity and pressure

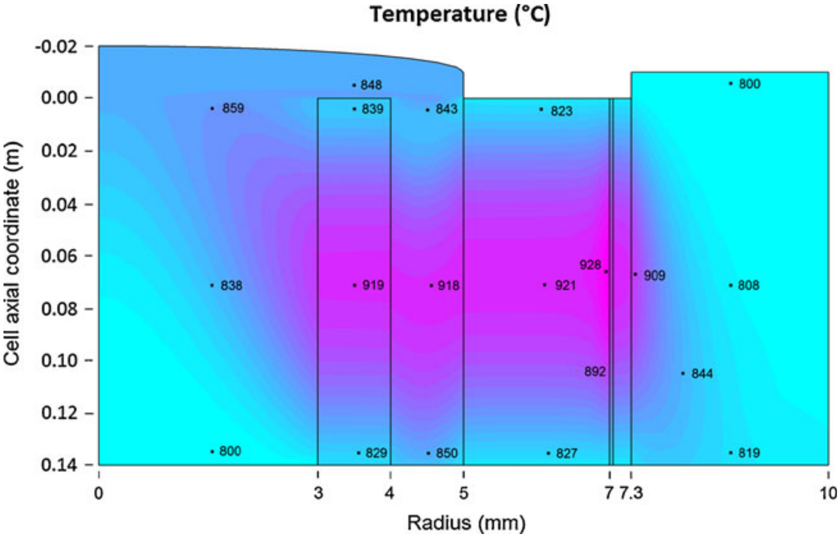

Fig. 10 Numerical results of temperature contour in pure hydrogen fueling operation

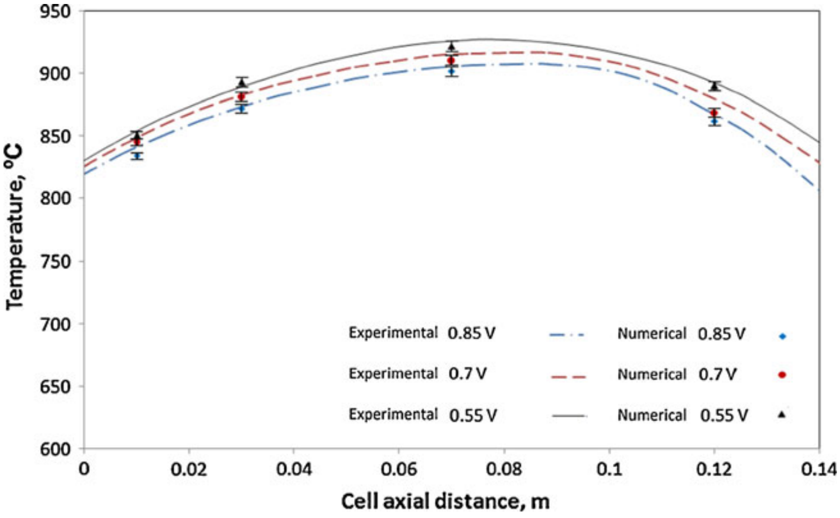

Fig. 11 Numerical results of temperature profile at electrolyte mid-thickness of the hydrogen fueled MT-SOFC at various cell voltages

fields and temperature distribution were the outputs of the simulation. The whole domain was discretized by 2,787 elements (2,680 quadrilateral elements and 107 triangular elements) which observed to be the minimum required number of elements through some mesh sensitivity verification trial runs. As shown in Fig. 5, the ratio of output result values for various element numbers to the values as the number of elements approaches to: ∞, would approach to unity for an element number of 2787. In this figure, the domain maximum temperature (T_{max}) and cell maximum radial current density (I_{max}) were chosen for mesh sensitivity case study.

Parameters

The parameters used to simulate the MT-SOFC are summarized in Table 3. Geometrical parameters such as porosity and density are typical of the selected manufacturing process for PEN layers. Physical parameters such as conductive, convective, and radiative heat transfer coefficients, gas diffusion coefficients, and electrochemical parameters are chosen as common values available in the literature. Constant values for the electrical conductivities of anode and cathode layers at the operating temperature range were considered. Due to the assumption of ideal current collection which implies low ohmic polarization, the resulting error for this assumption is negligible. The specified value for the fuel utilization factor is at the lower limit of common range for the type of SOFC in a single cell testing condition.

Results and discussion

Electrochemical performance

Steady state analysis of the developed model for the MT-SOFC with the cell voltage (DV) as a solution parameter

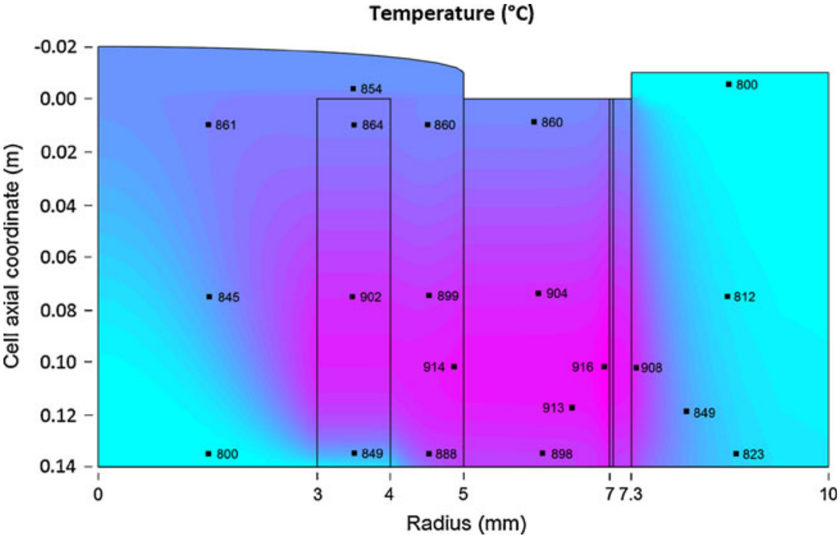

Fig. 12 Numerical results of temperature contour in GIR fueling operation

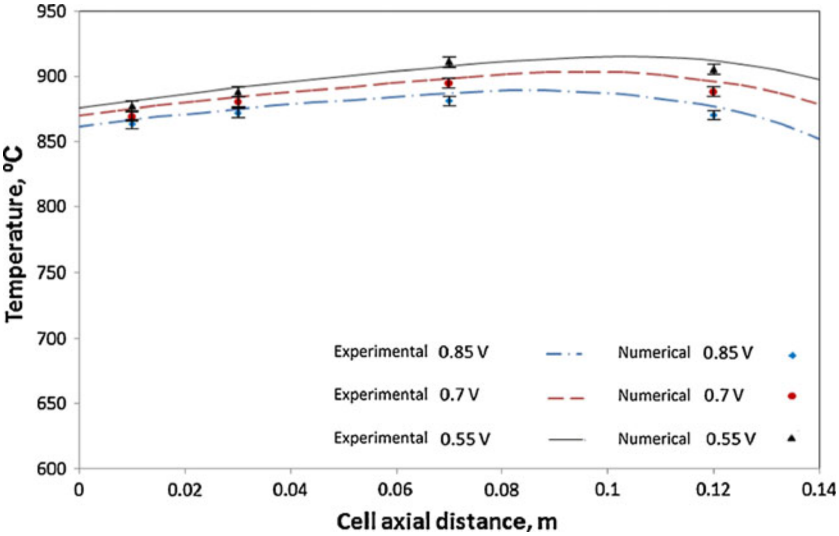

Fig. 13 Numerical results of temperature profile at electrolyte mid-thickness of the MT-SOFC in GIR fueling operation at various cell voltages

resulted in polarization curves shown in Fig. 6. In these curves, DV denotes the potential difference between the ideal cathode and anode current collectors. Also cell average current density (*I*) is defined as the total output current of the cell divided by cell active reaction area. Three fueling methods were considered as case studies: pure hydrogen, gradual internal reforming (GIR), and direct internal reforming (DIR). In GIR fueling method, the molar ratio of water steam to methane should be less than 0.1 whereas in DIR fueling method this ratio should be at least 1. Therefore, as shown in Table 3, the mole ratio of water steam to methane at input was chosen as: 0.094 and 1.23 for GIR and DIR fueling, respectively. The slope of polarization curve for pure hydrogen fueling case is lower than two other fueling cases. This is firstly due to lower operating temperature of the cell fueled by methane which is a consequence of endothermic internal reforming reaction. Secondly, the partial pressure of hydrogen in the pure hydrogen fueling operation is higher than two other cases in spite of more hydrogen content available to the electrochemical reaction in the methane fueling operations. This results in higher open circuit voltage as expressed by Eq. 7 and is apparent from the open circuit voltages of the polarization curves in Fig. 6. Lower operating temperature results in higher ohmic resistance of the electrolyte against ions flow and slower rate of electrochemical energy conversion. The slope of polarization curve in the case of DIR is lower than its slope in the case of GIR fueling, because of higher cooling action when input fuel comprises more water steam content which entails higher internal reforming rate.

In order to verify these simulation results, the prepared MT-SOFC was tested in the set up shown in Fig. 2. The furnace temperature was fixed to 800°C. This is the value

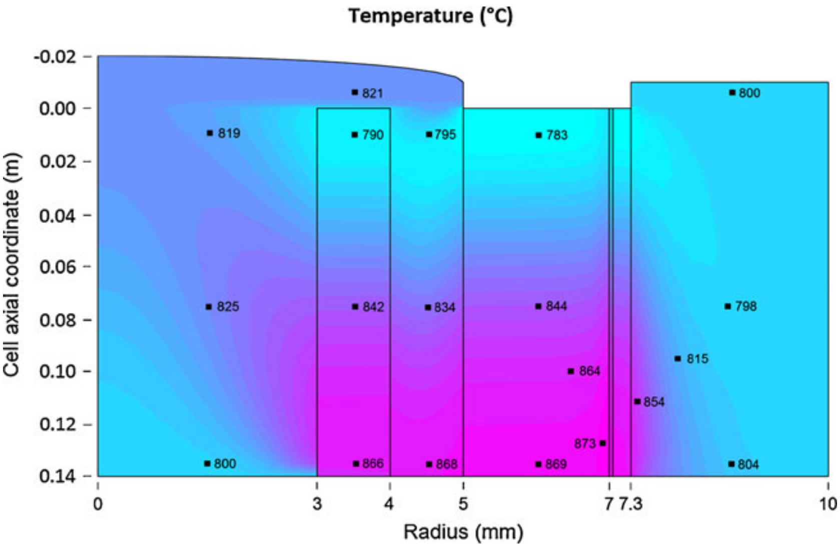

Fig. 14 Numerical results of temperature contour in DIR fueling operation

Fig. 15 Numerical results of temperature profile at electrolyte mid-thickness of the MT-SOFC in DIR fueling operation at various cell voltages

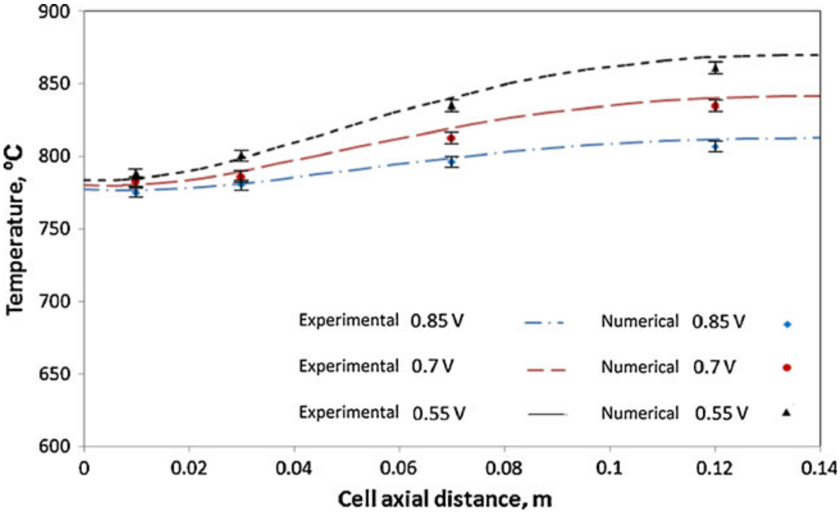

which was supplied to the model as input gas temperatures and ambient temperature in heat convection and radiation. In all points of the polarization curve nearly constant utilization factors of 0.4 and 0.17 were established for the fuel and air, respectively. The adopted fuel utilization factor is at the lower limit of the common range 0.45–0.85 for single MT-SOFCs [35]. For setting the considered values of utilization factors (Eqs. 39–42) were used:

$$U_{CH_4} = I/(4F) \tag{39}$$

$$U_{air} = I/(0.21(4F)) \tag{40}$$

$$n_{CH_4} = U_{CH_4}/UF_{CH_4} \tag{41}$$

$$n_{air} = U_{air}/UF_{air} \tag{42}$$

Where U_{CH_4}, U_{air} denote the molar rates of methane and air consumption in the electrochemical reaction; UF_{CH_4}, U_{air} are utilization factors for methane and air; and n_{CH_4}, n_{air} denote molar flow rates of input methane and air respectively. In each cell average current density during the test, the input gas flow rates were regulated to satisfy (Eqs. 39–42) for values of 0.4 and 0.17 as the fuel and air utilization factors. As shown in Fig. 6, there is an acceptable agreement between the simulation and experimental results. The deviation of experimental points from a smooth curve like the analytical polarization curve is due to errors in adjustment of input gasses utilization factors.

In Figs. 7 and 8, the radial current density distributions at the condition of 0.5 V cell potential, for the mentioned fueling methods are compared. In pure hydrogen fueling, the cell radial current density is maximized nearly at the

Fig. 16 Simulation results of species concentration in fuel channel of the MT-SOFC in hydrogen fueling method

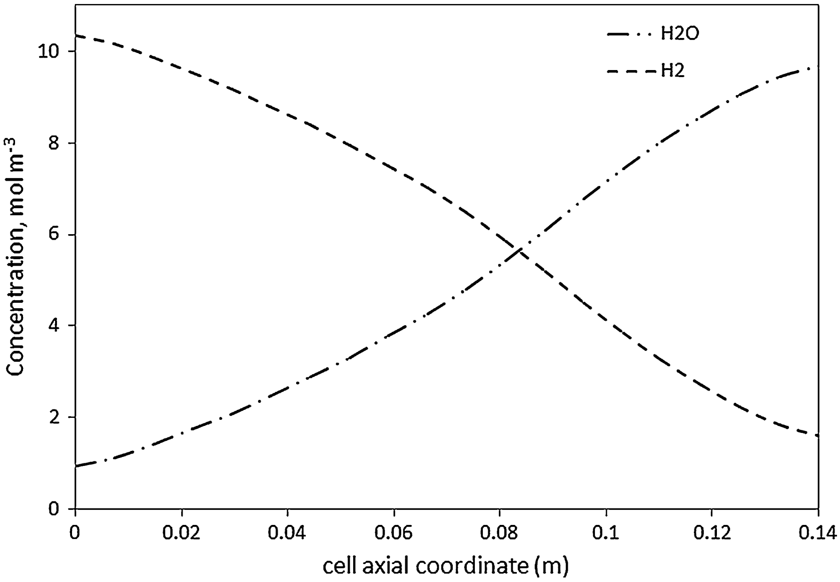

Fig. 17 Simulation results of species concentration in fuel channel of the MT-SOFC in GIR fueling method

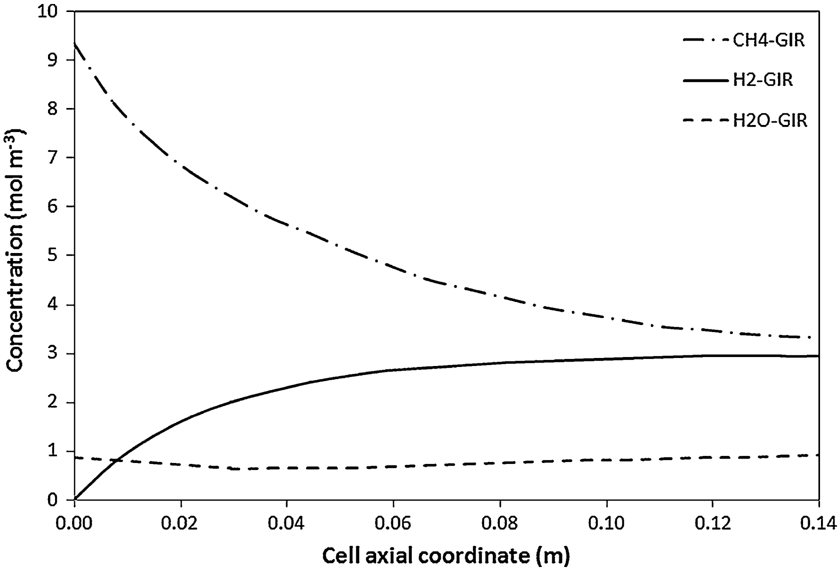

middle of the cell length. In GIR fueling case, the cell radial current density, first decreases near $z=0$ followed by increment towards the cell exit. The decrease of the cell radial current density at $z=0$ in the case of DIR fueling is more severe followed by an increase in the z direction at a higher rate compared with GIR fueling. As will be discussed in the next section, the temperature variation along the cell length is occurred in a similar form as the radial current density, so the increment of the radial current density at high temperature zones, can be attributed to the increase of the electrolyte ionic conductivity at these zones. Meanwhile increased current density at these zones, adds to the heat generation due to irreversibility of the electrochemical conversion as stated by Eq. 26.

Cell temperature distribution

Temperature profiles at the MT-SOFC electrolyte mid-thickness, for a cell voltage of: $DV=0.5$ V and various types of fueling (i.e., pure hydrogen, GIR, and DIR) are depicted in Fig. 9. Again the utilization factors were set to: 0.4 and 0.17 for fuel and air respectively. The characteristic of the profile curve for pure hydrogen is a maximum value at the cell middle length. For GIR fueling a gradual rise in the temperature until a maximum value near the cell output is perceived. In DIR fueling method the temperature of fuel at near $z=0$, is decreased sensibly due to cooling effect of reforming process, and then it increases until the maximum value at the cell output.

Fig. 18 Simulation results of species concentration in fuel channel of the MT-SOFC in DIR fueling method

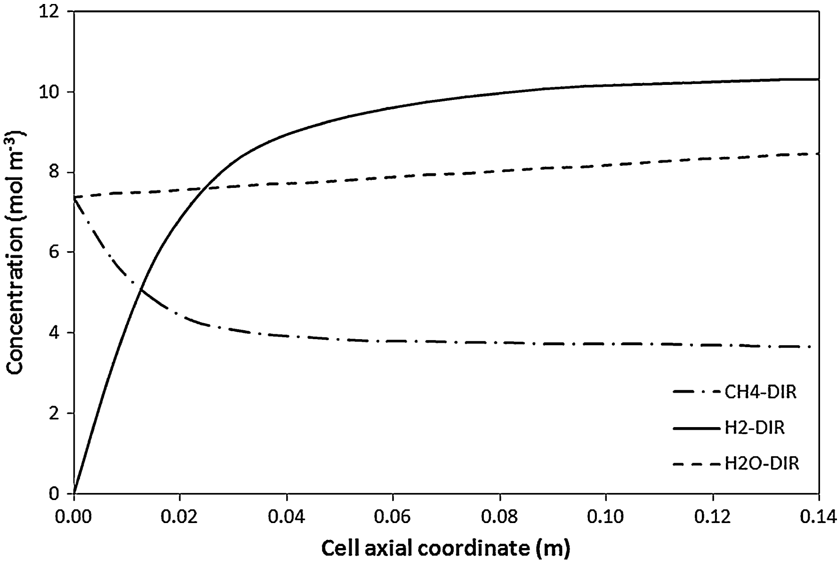

Temperature contour in all the solution subdomains are depicted in Fig. 10 for pure hydrogen fueling operation. In this case, heat generated from the irreversible electrochemical reaction causes progressive temperature rise in *z* direction until middle of the cell. As shown in Fig. 11, due to heat convection at MT-SOFC two ends, the maximum of electrolyte mid-thickness temperature profile is occurred at middle of the cell for various operating voltages.

Temperature contour of methane-fed MT-SOFC in GIR case is depicted in Fig. 12. In Fig. 13, the electrolyte mid-thickness temperature profiles for various cell voltages show gradual increases towards the exit of the cell and without a maximum at the middle. This can be explained by the endothermic nature of methane reforming reaction which utilizes the heat generated by electrochemical reaction.

In DIR fueling case, the input fuel contains enough water content to start the reforming reaction at the cell entrance. Whereas in the case of GIR fueling type, the required water steam for the reforming reaction should be supplied by the electrochemical reaction. Therefore, a decrease in the input fuel temperature is occurred in the DIR fueling method as is shown in the temperature contour of Fig. 14 and electrolyte mid-thickness temperature profiles of Fig. 15.

Concentration loss

The species concentration profiles along the inner wall of anode are depicted in (Figs. 16, 17, and 18). For the pure hydrogen fueling method, hydrogen concentration decreases in the *z* direction towards the cell output while water steam concentration increases in this direction (Fig. 16). The value of slope of these curves is maximum at the middle of the cell, where the temperature is maximum. At the location of maximum temperature, the electrochemical reaction rate is maximized. Therefore the rate of species consumption or production is a peak value, making the rate of the species concentration change with respect to the *z* as a maximum.

For the GIR fueling method, the concentration of hydrogen at the fuel entrance to the cell is negligible, but it increases gradually in the *z* direction due to reforming reaction which takes place in porous Ni-YSZ anode (Fig. 17). The concentration of methane is decreased gradually in the *z* direction due to this reforming reaction. The reason for gradual change of species in the *z* direction is insufficiency of water steam for progression of the reforming reaction. So, the required water steam is supplied from the electrochemical reaction of the cell making the concentration change in the *z* direction a gradual variation. Also water steam concentration is not increased sensibly in the *z* direction due to its consumption (in the reforming reaction) occurring in the right place of its production (electrochemical reaction layer).

In the DIR fueling method with surplus of water steam at the fuel entering into the cell, the rate of reforming reaction is considerably higher than its value in the GIR fueling method at the zone near $z=0$ (Fig. 18). Therefore, the reforming reaction is almost completed until $z=3$ cm. After that, the species concentrations change slowly in the *z* direction due to increase of product partial pressures and decrease of reactant partial pressures which retards the reforming reaction according to (Eqs. 30 and 31).

The concentration loss at each cell average current density (*I*) is equivalent to the resulting difference in V_{rev}^{A} when the value of species partial pressures in Eq. 7 are

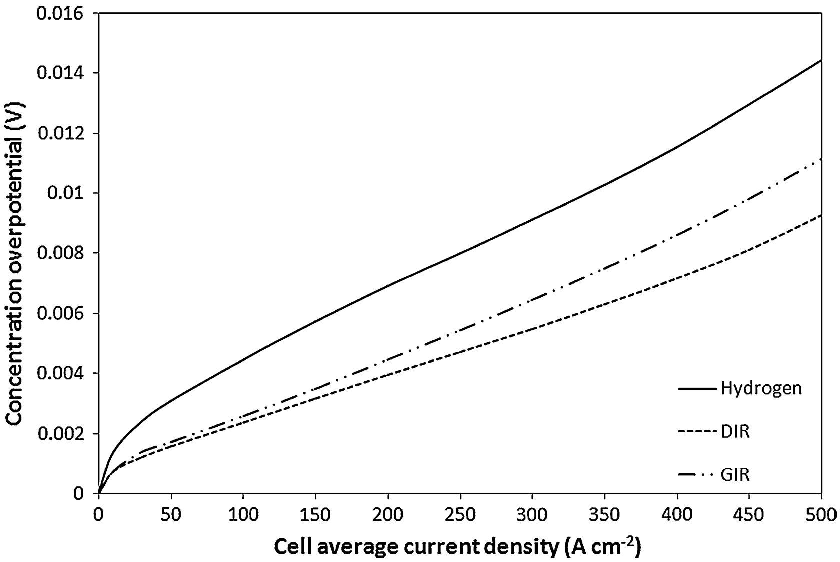

Fig. 19 Numerical results of the MT-SOFC concentration overpotential in various fueling types

replaced with their amount in the anode inner wall (subjected to fuel channel flow stream) at the same *z* coordinate. The computed concentration losses in three mentioned varieties of fueling methods are compared in Fig. 19. In the pure hydrogen fueling operation, hydrogen concentration diminishes in the direction of anode layer depth. Whereas, in the DIR and GIR fueling operations there is redundancy of hydrogen which is produced within the porous anode to the amount more than its consumption in the electrochemical reaction layer. The DIR fueling method is even superior to the GIR fueling method in this regard, since there is excess hydrogen supply to the electrochemical reaction zone in the DIR method. This phenomena is distinct from the one stated about different partial pressures in "Electrochemical performance" for three fueling methods. The concentration loss accounts for the gradient of V_{rev}^{A} in the anode thickness direction. Although the absolute value of this term also shows a similar trend and is lower in methane-fed cells than the pure hydrogen fueling case due to the existence of CO_2 and unreformed CH_4 in addition to H_2O in the anode electrochemical reaction zone. In addition, in DIR fueling operation in which hydrogen production rate is higher than GIR fueling operation, lower concentration polarization is estimated.

Conclusions

A mathematical model was developed for the prediction of performance, thermal effects, and the behavior of direct internal reforming in MT-SOFC. In this model, temperature dependence of the electrochemical reactions was considered that resulted in variation in polarization curve shapes. In pure hydrogen fueling method, the temperature profile has a maximum value at middle of the cell, whereas in GIR and DIR fueling methods the maximum value is shifted to the cell exit.

In hydrogen fueling case, the polarization curve has lower slope than other two fueling methods which can be attributed to higher operating temperature of the cell and higher partial pressure of hydrogen at the electrochemical reaction zone which results in higher Nernst voltage.

Concentration loss of a MT-SOFC in methane DIR reforming mode is lower than two other fueling cases, since in this case there is surplus of hydrogen production within the anode layer which diminishes the Nernst voltage gradient in the anode thickness direction. The highest concentration loss is perceived in pure hydrogen fed cell because hydrogen should diffuse into the reaction layer from the fuel channel without any production.

The validity of the developed model was verified through some simple temperature and polarization curve measurements. There is acceptable agreement between experimental and analytical results regarding heat transfer and electrical models. More detailed study on the validation of the electrochemical model presented by (Eqs. 11–15) is suggested as an extension to this research.

Acknowledgment The authors gratefully acknowledge support and assistance of manufacturing technology center of department of mechanical engineering, Iran University of Science and Technology (IUST).

References

1. Steele BCH, Heinzel A (2001) Nature 414:345
2. Anonymous (2007) Journal of Power Sources 169:315–326
3. Lawlor V, Griesser S, Buchinger G, Olabi AG, Cordiner S, Meissner D (2009) J Power Sources 193:387–399
4. Van Herle J, Ihringer R, Sammes NM, Tompsett G, Kendall K, Yamada K, Wen C, Kawada T, Ihara M, Mizusaki J (2000) Solid State Ionics 132:333–342
5. Anonymous (2009) Journal of Power Sources 193:241–248
6. Kendall K et al (2002) J Power Sources 106:323–327
7. Staniforth J, Kendall K (2000) J Power Sources 86:401–403
8. Sánchez D, Chacartegui R, Muñoz A, Sánchez T (2008) Int J Hydrogen Energy 33:1834–1844
9. Dokmaingam P, Irvine JTS, Assabumrungrat S, Charojrochkul S, Laosiripojana N (2010) Int J Hydrogen Energy 35:13271–13279
10. Dokamaingam P, Assabumrungrat S, Soottitantawat A, Sramala I, Laosiripojana N (2009) Int J Hydrogen Energy 34:410–421
11. Aguiar P, Chadwick D, Kershenbaum L (2002) Chem Eng Sci 57:1665–1677
12. Ding OL, Chan SH (2008) Int J Hydrogen Energy 33:633–643
13. Vernoux P, Guindet J, Kleitz M (1998) J Electrochem Soc 145 (10):3487–3492
14. Georges S, Parrour G, Henault M, Fouletier J (2006) Solid State Ionics 177:2109–2112
15. Lehnert W, Meusinger J, Thom F (2000) J Power Sources 87:57–63
16. Suwanwarangkul R, Croiset E, Fowler MW, Douglas PL, Entchev E, Douglas MA (2003) J Power Sources 122:9–18
17. Aguiar P, Adjiman CS, Brandon NP (2004) J Power Sources 132:113–126
18. Klein J-M, Bultel Y, Georges S, Pons M (2007) Chem Eng Sci 62:1636–1649
19. Ho TX, Kosinski P, Hoffmann AC, Vik A (2008) Chem Eng Sci 63:5356–5365
20. Chung C-Y, Chung Y-C (2005) J Power Sources 154:35–41
21. Ji Y, Yuan K, Chung JN, Chen Y-C (2006) J Power Sources 161:380–391
22. Cui D, Liu L, Dong Y, Cheng M (2007) J Power Sources 174:246–254
23. Suwanwarangkul R, Croiset E, Pritzker MD, Fowler MW, Douglas PL, Entchev E (2006) J Power Sources 154:74–85
24. Nield DA, Bejan A (1999) Convection in porous media, 2nd edn. Springer, New York
25. Hussain MM et al (2006) J Power Sources 161:1012–1022
26. Costamagna P, Costa P, Antonucci V (1998) Electrochim Acta 43:375–394
27. COMSOL Ltd, FEMLAB®, Version 3.4 User's Guide, Copyright 1994–2007 by COMSOL AB. Available at: http://www.femlab.ch.
28. Chan SH, Khor KA, Xia ZT (2001) J Power Sources 93:130–140
29. Massoud Kaviany (1995) Principles of heat transfer in porous media (mechanical engineering series), second edition (ISBN: 0387945504/0-387-94550-4). Springer, Berlin

30. Hagiwara A, Michibata H, Kimura A, Jaszcar MP, Tomlins GW, Veyo SE (1999) Proceedings of the 3rd International Fuel Cell Conference, Nagoya, Japan. pp. 365–368
31. Nagata S, Momma A, Kato T, Kasuga Y (2001) J Power Sources 101:60–71
32. Mollayi Barzi Y, Ghassemi M, Hamedi MH (2009) Int J Hydrogen Energy 34:2015–2025
33. Singhal SC, Kendall K (1995) High temperature solid oxide fuel cells: fundamentals, design and applications. Elsevier, Amsterdam, pp 83–92
34. Ho TX, Kosinski P, Hoffmann AC, Vik A (2009) Chem Eng Sci 64:3000–3009
35. Lee S-B, Lim T-H, Song R-H, Shin D-R, Dong S-K (2008) Int J Hydrogen Energy 33:2330–2336